Asociación Argentina
de Mecánica Computacional

Mecánica Computacional Vol XXIX, págs. 5941-5951 (artículo completo)
Eduardo Dvorkin, Marcela Goldschmit, Mario Storti (Eds.)
Buenos Aires, Argentina, 15-18 Noviembre 2010

COMPUTATIONAL AND EXPERIMENTAL HEMODYNAMIC ANALYSIS OF AN INTRACRANIAL ANEURYSM

Marcelo Raschi[a], Fernando Mut[a], Rainald Löhner[a], Christopher M. Putman[b], Fernando Viñuela[c], Satoshi Tateshima[c], Kazuo Tanishita[d], and Juan R. Cebral[a]

[a]*Center for Computational Fluid Dynamics, George Mason University, Fairfax, Virginia, USA*
mraschi@gmu.edu

[b]*Interventional Neuroradiology, Inova Fairfax Hospital,Falls Church, Virginia, USA*

[c]*Interventional Neuroradiology, UCLA Medical Center, Los Angeles, California, USA*

[d]*IDepartment of Systems Design Engineering, Keio University, Tokyo, Japan*

Keywords: Hemodynamics, Cerebral Aneurysms, Computational Fluid Dynamics, Particle Image Velocimetry.

Abstract. Hemodynamics is thought to play a fundamental role in the mechanisms of cerebral aneurysm formation, growth, and either stabilization or rupture. Understanding these mechanisms is important to improve current diagnosis and treatment of intracranial aneurysms. The purpose of this study was to analyze the blood flow field in a growing cerebral aneurysm using experimental particle image velocimetry (PIV) and computational fluid dynamics (CFD) techniques. Patient-specific models were constructed from 3D computed tomography angiography (CTA) images acquired at one-year intervals during a conservative follow up period. Physical silicone models were constructed from the CTA images using rapid prototyping techniques and the pulsatile blood flow fields were measured with PIV. Corresponding CFD models were created and run under pulsatile flows matching the experimental flow conditions. For comparison, the PIV and CFD models were aligned and the corresponding flow fields interpolated to a common grid covering the aneurysm volume. The blood flow fields were then visualized and compared qualitatively by inspection and quantitatively by defining a similarity measure between the PIV and CFD vector fields. The results indicate that the experimental and computational flow fields are in good agreement. Specifically, both techniques yield consistent qualitative representations of the major characteristics of the inflow stream and the intra-aneurysmal flow structures, and their change during the geometric evolution of the aneurysm. Additionally, the PIV and CFD flow fields exhibit a degree of coincidence of over 80% in the aneurysm interior. However, as expected, differences between the experimental and computational results were observed in the regions near the aneurysm wall. Differences in the magnitudes of the CFD and PIV velocities were also observed. Possibly, these differences could be attributed to the limited resolution of the experimental measurements and to imperfect match of the flow boundary conditions. Despite these differences and the inherent limitations of both techniques, the information derived from these complementary models is consistent and can be used to study the role of hemodynamics in the mechanisms of aneurysm pathogenesis and progression.

1 INTRODUCTION

Stroke is the most common life-threatening neurological disease and is the third leading cause of death in the United States, after heart disease and cancer. Non-traumatic subarachnoid hemorrhage (SAH) constitutes approximately 5-10% of all strokes, and roughly 80% of SAH results from rupture of a brain aneurysm (Kassell and Torner 1983; Weir and Macdonald 1996). Autopsy studies estimate that as much as 5% of the population may harbor undiscovered brain aneurysms (Wiebers, Torner et al. 1992; Rinkel, Djibuti et al. 1998). The fatality rate in aneurysmal rupture remains high (45% overall during the first year) (Wiebers, Torner et al. 1992). In more than half of survivors, the level of disability is major, and 64% of those patients never achieve the quality of life they enjoyed before the aneurysm ruptured (Kelly, Stein et al. 1983; Ropper and Zervas 1984). Whether unruptured brain aneurysms should be treated has been debated for the last decade (Juvela, Porras et al. 1993; Murayama, Vinuela et al. 1999; Tsutsumi, Ueki et al. 2000; Wiebers, Whisnant et al. 2003). This is particularly true in aneurysms less than 12 mm in the greatest diameter (Wiebers, Whisnant et al. 2003). Recent developments in neuroimaging have detected more incidental brain aneurysms in routine clinical practice. Planning elective surgery requires a better understanding of the process of aneurysm formation, progression, and rupture so that a sound judgment between the risks and benefits of possible therapies can be made.

Hemodynamics is thought to play a fundamental role in the mechanisms of cerebral aneurysm formation, growth, and stabilization or rupture (Sforza, Putman et al. 2009). Understanding these mechanisms is important to improve current diagnosis and treatment of intracranial aneurysms. Most previous studies of the hemodynamics of cerebral aneurysms have been limited to aneurysms imaged only once (Shojima, Oshima et al. 2004; Cebral, Castro et al. 2005; Valencia, Morales et al. 2008). However, in order to improve our knowledge of the mechanisms governing the evolution of cerebral aneurysms it has become necessary to analyze aneurysms that have been longitudinally followed during their natural evolution (Boussel, Rayz et al. 2008).Thus, the purpose of this study was to analyze and compare the blood flow fields in a growing cerebral aneurysm obtained by experimental particle image velocimetry (PIV) and computational fluid dynamics (CFD) techniques.

2 METHODS

2.1 Imaging Data

An intracranial aneurysm with documented growth was selected from a database of unruptured, untreated cerebral aneurysms longitudinally followed with non-invasive imaging. Aneurysms in this database are classified as growing if any of their dimensions changes by at least 0.5 mm, as determined by experienced neuroradiologists. The selected aneurysm was imaged at one year intervals for four

years using computed tomography angiography (CTA). Because the aneurysm was growing it was subsequently treated endovascularly with coils. The aneurysm was located in the anterior communicating artery (Acom). Typically, aneurysms in this location receive blood from two sources, the left and the righ A1 segments of the anterior cerebral arteries (ACA). However, in this particular patient, the aneurysm only accepts blood from the left A1, the contralateral (right) A1 is missing (hypoplastic or aplastic). Figure 1 shows volume renderings of the 3 longitudinal CTA images used in this study.

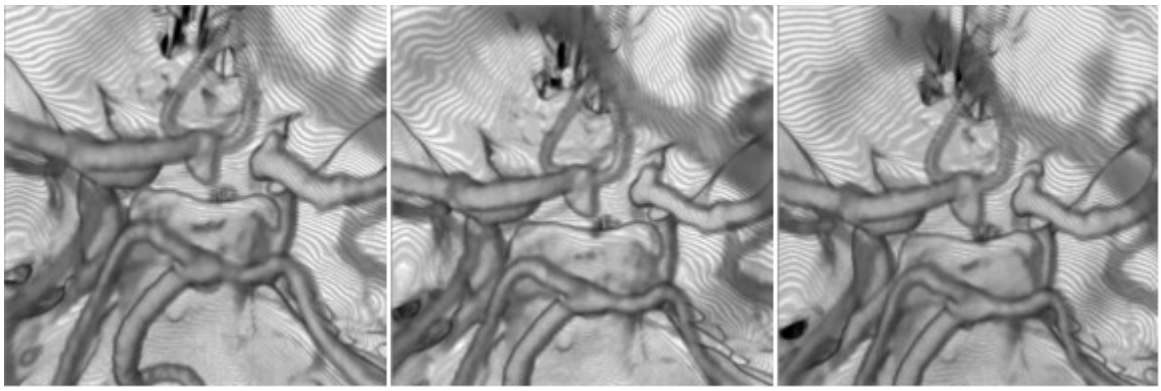

Figure 1: 3D volumen rendered images of Acom aneurysm longitudinally followed with CTA at 1 year intervals.

2.2 In Vitro Modeling

The aneurysm and connected arteries were manually segmented from the CTA images corresponding to each examination during the observation period. The resulting surfaces were saved in STL format (shown in Figure 2) and used to build corresponding rigid silicon models using rapid prototyping techniques and a scale of 3:1 with respect to the in vivo anatomical dimensions. These models were placed in a pulsatile flow loop and the velocity field was measured using particle image velocimetry (PIV). The PIV system comprises a laser sheet for the visualization of 1 mm thick plane of the flow field, trigged at intervals of 150μs, and a CCD camera with a resolution of 1376x1040 pixels. The velocity vector field was calculated from the double-frame acquired imaged based on the path of the particle. The fluid used was a glycerin solution of 58% by weight, with a viscosity μ= 0.0082 Pa.s, density ρ=1140 kg/m^3, and a refractive index n=1.41, matching the refractive index of the silicon resin of the model. The pulsatile flow conditions were derived from in vivo ultrasound measurements of flow velocities in ACA's of normal subjects (Hennerici, Rautenberg et al. 1987). The Reynolds number based on the ACA diameter varied in the range of 450-800 and the Womersley number was set to 2.7. The in-plane components of the flow velocity were measured on two sets of orthogonal planes separated by 1.0 mm at four instants of time during the cardiac cycle. The sets consisted in 19 planes perpendicular to the *x*-direction and 15 planes perpendicular to the *y*-direction. Each plane has a resolution of 43x32 points, and the separation between points is 0.82 m in

each direction for the first set and 0.78 mm for the second set.

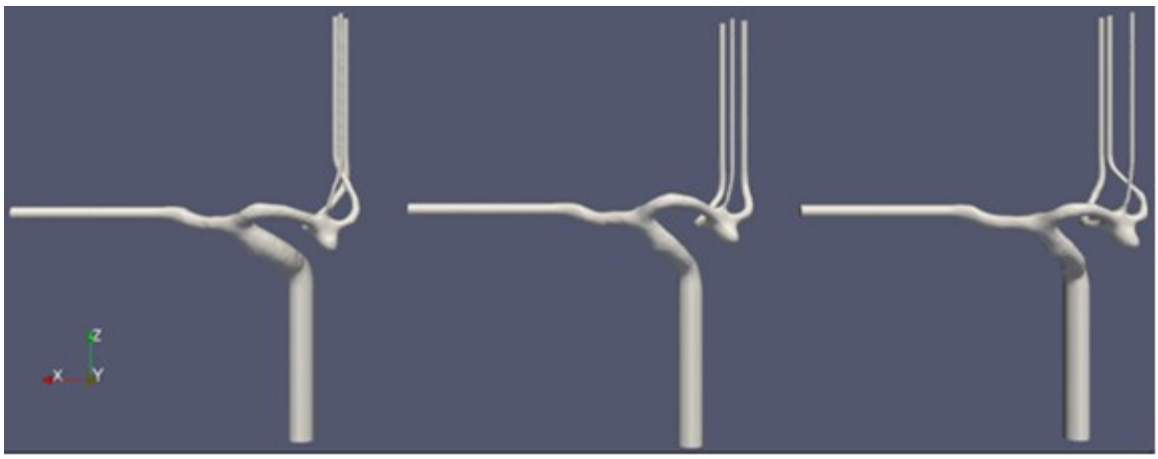

Figure 2: vascular reconstructions (STL surface models) used to build in vitro and computational models corresponding to each of the observation points shown in Figure 1.

2.3 Computational Fluid Dynamics Modeling

Computational fluid dynamics models of the aneurysm at each stage of its evolution were created from the corresponding STL surfaces. Unstructured grids composed of tetrahedral elements were generated using an advancing front technique and a minimum resolution of 0.02 cm (Löhner 2001; Cebral, Castro et al. 2005). The resulting grids contained approximately 1.92 million, 1.77 million and 1.84 million elements, respectively. Blood flows are mathematically modeled using the unsteady 3D Navier-Stokes equations for an incompressible Newtonian fluid. The governing equations are advanced in time using a fully implicit scheme that recasts the original equations as a steady-state problem in pseudo-time (ϑ) at each time-step (n):

$$u^{\xi}_{,\vartheta} + u^{\xi} \cdot \nabla u^{\xi} + \nabla p^{\xi} = \nabla \eta \, \nabla u^{\xi} - \frac{u^{\xi} - u^{n}}{\xi \, \Delta t} \tag{1}$$

$$\nabla \cdot u^{\theta} = 0 \tag{2}$$

where u is the velocity, p the pressure, η the kinematic viscosity, u^n denotes the velocity at the previous timestep and $u^{\xi}=(1-\xi)\, u^{n} + \xi \, u^{n+1}$. These equations are solved using a pressure-projection method where the spatial discretization is carried out using an edge-based upwind finite element method (Löhner 2001). The discretized momentum equation is solved using a Generalized Minimal Residuals (GMRES) method and the discretized pressure Poisson equation is solved using an efficient deflated preconditioned conjugate gradients method (Mut, Aubry et al. 2009). The CFD simulations were carried out by matching the Reynolds and Womersley numbers of the in vitro experiments. A fully developed Womersley profile was used to impose pulsatile boundary conditions at the model inlet. Traction-free boundary conditions were prescribed at the outlets and no-slip boundary conditions on the vessel walls. The pulsatile simulations were carried out using 100 timesteps per cardiac cycle, for a

total of two cardiac cycles. Results are presented for the second cycle.

2.4 Comparison

The two orthogonal PIV measurements of the flow velocity were used to recover a 3D velocity field. Both sets of planes were interpolated and combined into a new data set. The combined volume was limited to the intersection of both sets, as it was necessary to have information of both velocity directions. All the points within the combined volume were considered. Each component of the velocity was linearly interpolated to each point and the *z*-component was averaged between the two original sets. This new 3D PIV velocity field was manually aligned with the CFD model, and the velocity was interpolated to the points from the CFD grid. For the comparison of flow patterns, two simple indeces for measuring the similarity of the velocity fields were defined: angular and magnitude similarity. Angular similarity is the cosine of the angle subtended between each vector $\mathbf{V}_{PIV}.\mathbf{V}_{CFD}/(V_{PIV}.V_{CFD})$, where V=mag($\mathbf{V}$). The scale varies in the range [-1,1], being 1 the highest similarity. The second index accounts for the magnitude similarity, it is based on the absolute difference between normalized velocities and is defined as $1-|V_{PIV}/\max(V_{PIV})-V_{CFD}/\max(V_{CFD})|$, which varies in the range [0,1], 1 being the most similar. Global similarity measures are then obtained from the point-to-point similarity indeces as the volume integral of angular and magnitude similarities over the volume in region of interest.

3 RESULTS

The CFD and PIV flow fields for the three geometric models (denoted as models #1, #2 and #3, respectively) of the aneurysm were compared at four time instants during the cardiac cycle. Time points t1 to t4 of the PIV measurement correspond with timesteps 20, 35, 65 and 95 of the CFD simulations, respectively. Times t2 and t4 correspond to systole and diastole phases of the cardiac cycle.

Qualitative comparison: Visualizations of the intra-aneurysmal flow patterns at peak systole for all aneurysm geometries obtained with CFD and PIV are presented in Figure 3. These visualizations show a good qualitative agreement between the flow fields obtained with both techniques at each stage during the evolution of the aneurysm as well as its change as the aneurysm growths. It can be seen that as the aneurysm enlarges the main flow structure becomes more elongated. Additionally, the flow recirculation region shows a change in the direction of its axis and a slight translation and enlargement. The main flow structures and their variation during the aneurysm progression observed with both PIV and CFD techniques are consistent. However, it is noticeable in all models that PIV streamlines stop near the wall and that CFD velocities tend to be larger in the inflow regions near the wall.

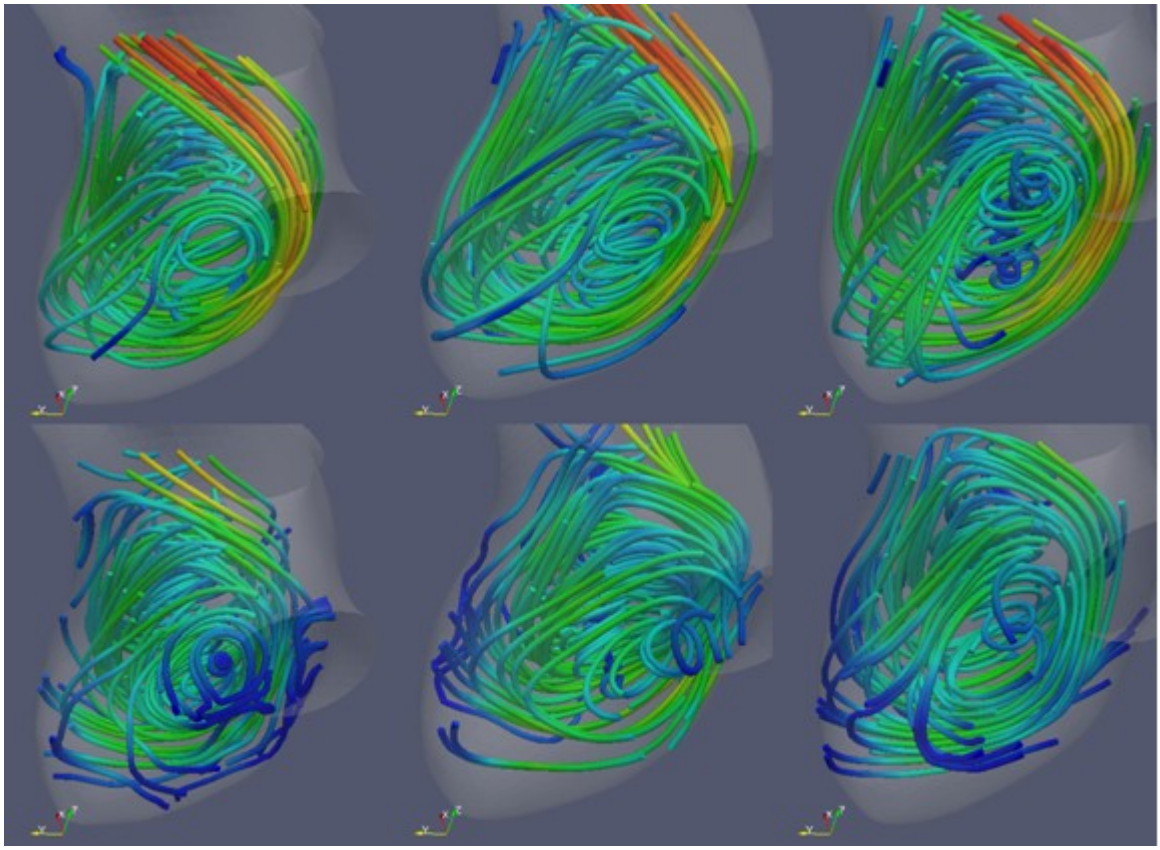

Figure 3: Streamlines of fluid structure for CFD calculation (top) and PIV measurements (bottom), for the models #1, #2, and #3 (left to right) at time t2 corresponding to the systole.

Sets of cut planes were defined for all the models and at all four time instants t1-t4 for visualizing the major flow structures, captured with PIV and CFD. The cut planes in Figure 4 show the magnitude of the velocity for model #1 at the time t2. Although the main flow structures are consistent, differences between the CFD and PIV flow fields can be observed in the near wall regions. PIV seems to underresolve the thin inflow jet when it flows parallel to the wall near the impingment region. The effect of underresolving the flow in the region close the wall is more noticeable in the leftmost cut-plane of Figure 4, which is almost completely defined near the wall.

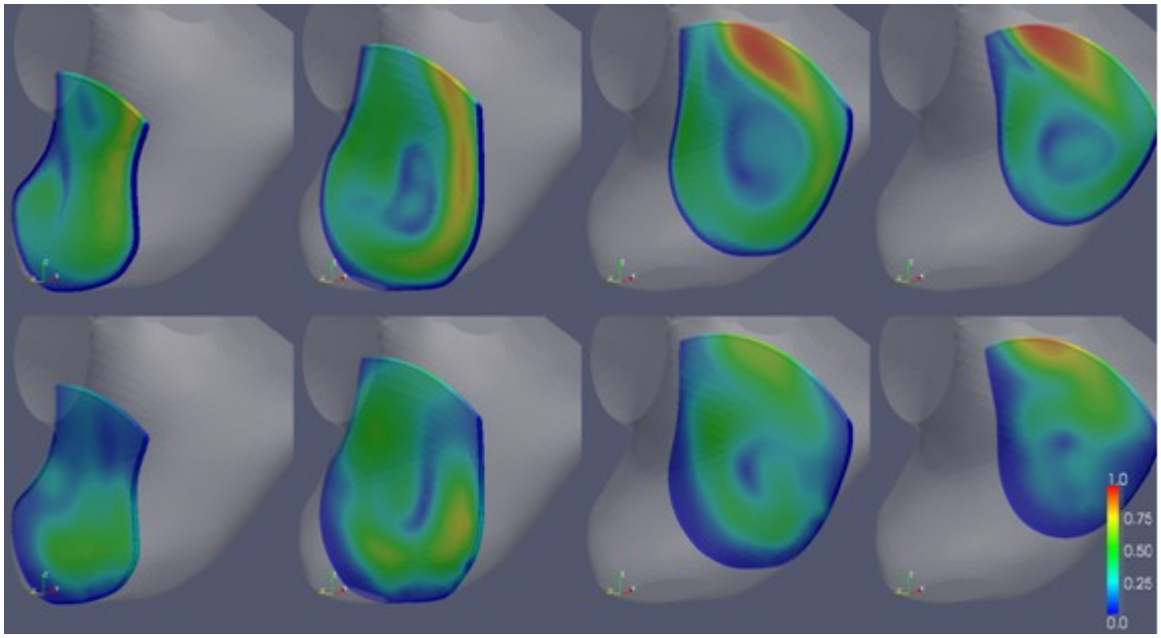

Figure 4: Cut-planes of the model #2 at time t2 showing the magnitude of the normalized velocity for CFD (top) and PIV (bottom). All of the PIV planes, particularly the leftmost plane, show important differences, as compared to the CFD planes, in the region near the wall.

Quantitative comparison: The local distribution of angular and magnitude similarities described before are presented for model #1 on a set of cut-planes at time t2 in Figure 5. These visualizations suggest that the CFD and PIV flow fields are in good agreement in the inner region of the aneurysm, except for a small central region where differences in the velocity directions can be observed. Note however that the velocity in this central region is quite small and thus large differences in vector directions can be expected. Additionally, these visualizations show that there are differences in the velocity magnitudes close to the wall along the inflow stream.

Since PIV measurements are known to have difficulties in the near wall regions the effect of measurement errors near the wall on the global similarity was studied. For this purpose, the global similarity was computed for smaller inner volumes, obtained by excluding outer shells of increasing thickness. Shells of thickness 0.25d, 0.50d, 1.00d, and 1.50d were excluded, where d=0.8 mm is the average point separation of the PIV measurement. Figure 6 shows angular and magnitude similarities for the four reduced volumes.

Finally, the global angular and magnitude similarities for all models and times are presented in Figure 7. The different bars represent the values corresponding to excluding near wall shells of increasing thickness.

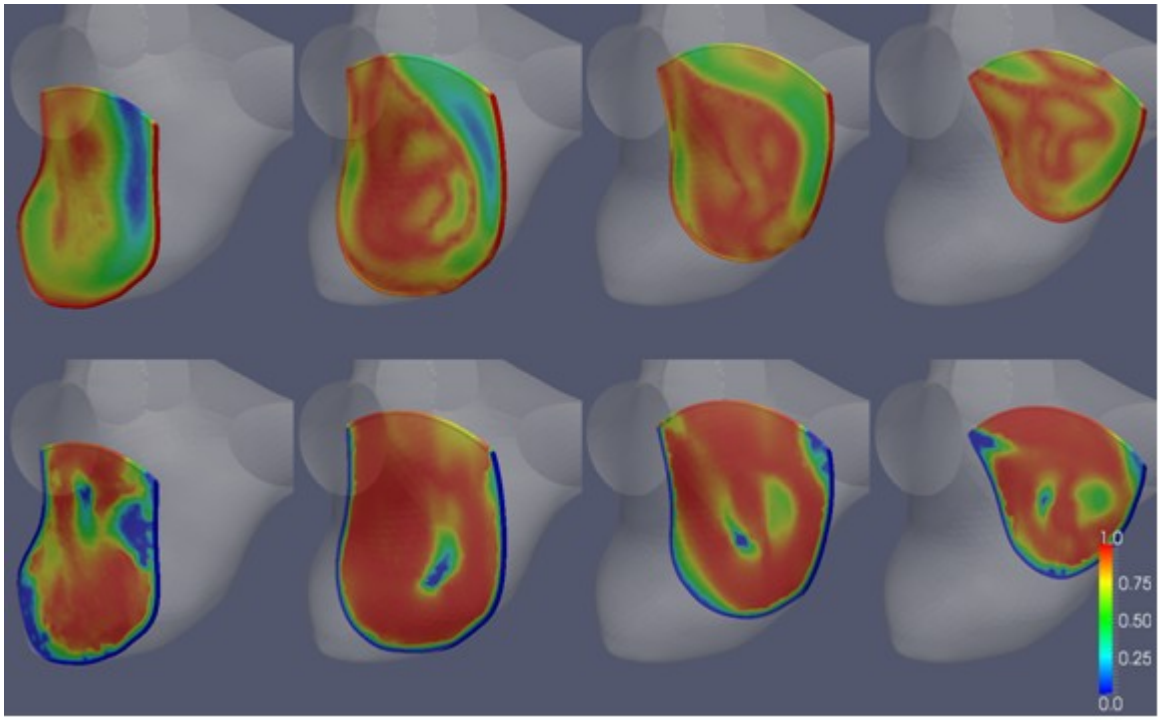

Figure 5: Cut-planes showing magnitude (top) and angle (bottom) similarity for model #1 at time t2.

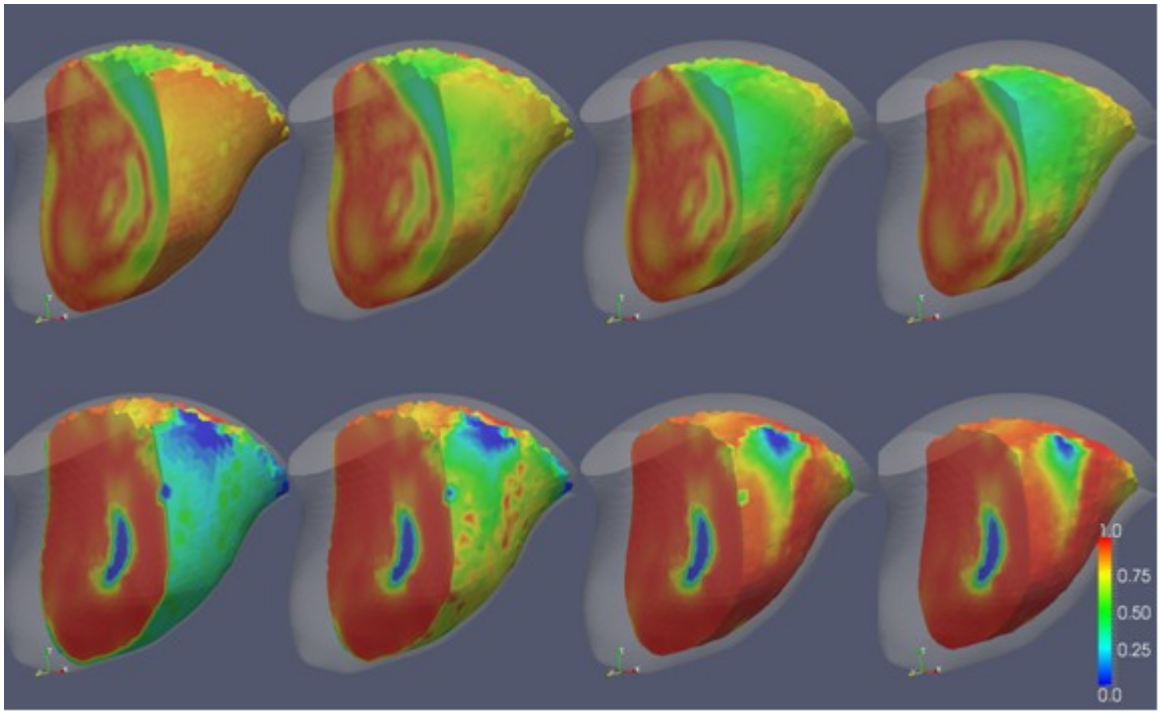

Figure 6: Magnitude (top) and angular (bottom) similarity for model #1 at time t2, computed for reduced volumes. From left to right, the excluded shell thickness is 0.25*d*, 0.50*d*, 1.00*d*, and 1.50*d*.

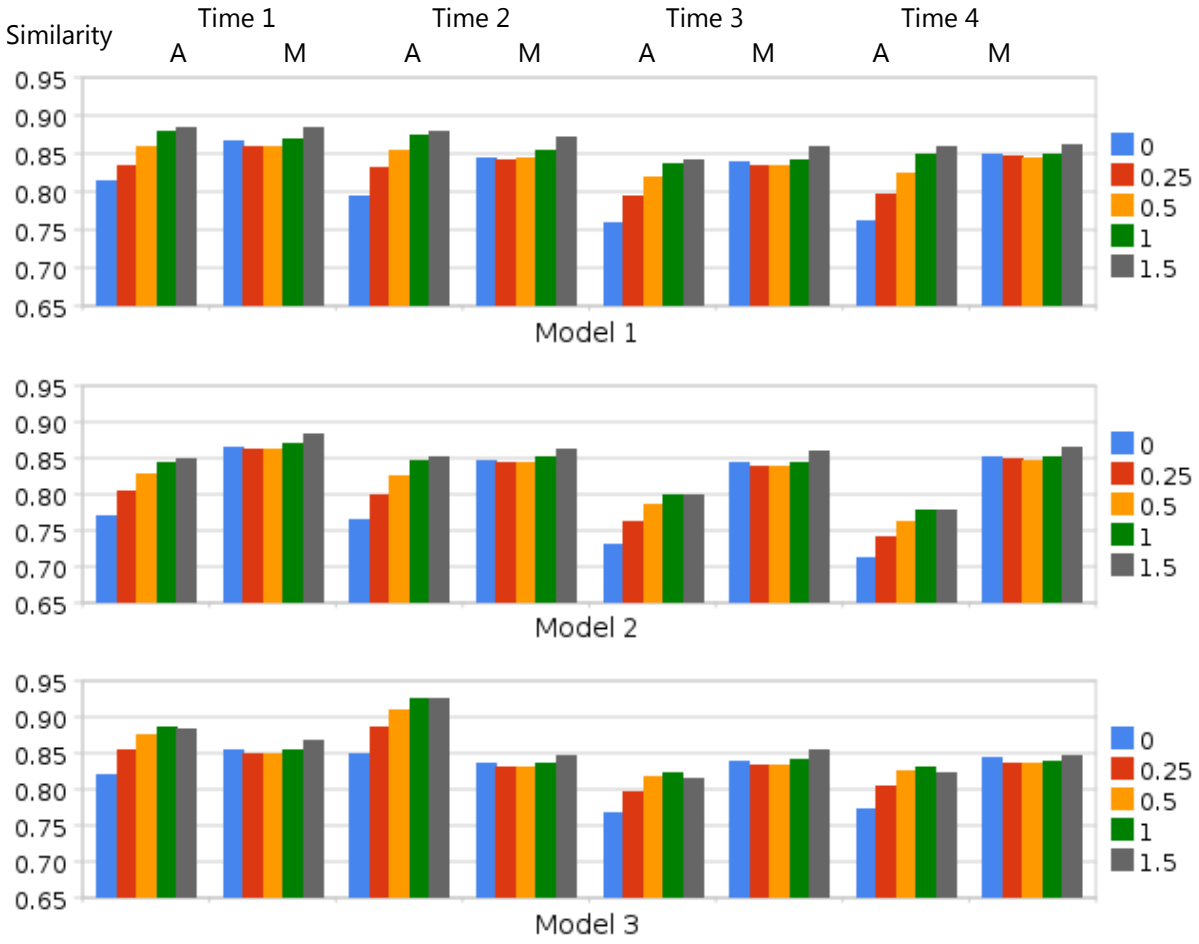

Figure 7: Global angular (A) and magnitude (M) similarity obtained for original (0*d*) and reduced volumes (0.25*d*, 0.50*d*, 1.00*d*, and 1.50*d*).

For each case, there seems to be an asymptotic similarity value between 0.8 and 0.9 after reducing the effect of the low velocities near the wall. In most cases, the similarity is greater than 0.8 after reducing the volume by a distance of 1*d*. Such reduction of volume could be seen as excluding the most external "pixel" of the PIV measurement. These results suggest that there is an 80% of agreement between numerical simulations and experimental measurements for regions of the aneurysm that exclude an outer shell of a thickness comparable to the resolution of the PIV system. If this layer near the wall is not discarded the magnitude similarity drops to about 75%.

4 CONCLUSIONS

The blood flow fields of a growing intracranial aneurysm obtained experimentally using PIV and computationally using CFD were found to be in good agreement. Specifically, both techniques yield consistent qualitative representations of the major characteristics of the inflow stream and the intra-aneurysmal flow structures, and

their change during the evolution of the aneurysm. Additionally, the PIV and CFD flow fields exhibit a degree of coincidence of over 80% in the aneurysm interior. As expected, differences between the experimental and computational results were observed in the regions near the aneurysm wall. Despite these differences and the inherent limitations of each technique, the information derived from these complementary models is consistent and can be used to study the role of hemodynamics in the mechanisms of aneurysm pathogenesis and progression.

ACKNOWLEDGEMENTS

We thank Philips Medical Systems and the National Institutes of Health (grant # R01NS059063) for financial support.

REFERENCES

Boussel, L., V. Rayz, et al. Aneurysm growth occurs at region of low wall shear stress: patient-specific correlation of hemodynamics and growth in a longitudinal study. *Stroke*, 39(11): 2997-3002, 2008.

Cebral, J. R., M. A. Castro, et al. Efficient pipeline for image-based patient-specific analysis of cerebral aneurysm hemodynamics: Technique and sensitivity. *IEEE Transactions in Medical Imaging*, 24(1): 457-467, 2005.

Cebral, J. R., M. A. Castro, et al. Characterization of cerebral aneurysm for assessing risk of rupture using patient-specific computational hemodynamics models. *AJNR American Journal of Neuroradiology*, 26: 2550-2559, 2005.

Hennerici, M., W. Rautenberg, et al. Transcranial Doppler ultrasound for the assessment of intracranial arterial flow velocity--Part 1. Examination technique and normal values. *Surg Neurol*, 27(5): 439-48, 1987.

Juvela, S., M. Porras, et al. Natural history of unruptured intracranial aneurysms: a long-term follow-up study. *Journal of Neurosurgery*, 79: 174-182, 1993.

Kassell, N. F. and J. C. Torner. Aneurysmal rebleeding: a preliminary report from the Cooperative Aneurysm Study. *Neurosurgery*, 13: 479-481, 1983.

Kelly, P. J., J. Stein, et al. Functional recovery after rehabilitation for cerebellar stroke. *Stroke*, 32: 530-534, 1983.

Löhner, R. *Applied CFD techniques*, John Wiley & Sons, 2001.

Murayama, Y., F. Vinuela, et al. Embolization of incidental aneurysms by using the Guglielmi detachable coil system. *Journal of Neurosurgery*, 90: 207-214, 1999.

Mut, F., R. Aubry, et al. Fast numerical solutions in patient-specific simulations of arterial models. *Comm Num Meth Eng*, DOI 10.1002/cnm.1235, 2009.

Rinkel, G. J., M. Djibuti, et al. Prevalence and risk of rupture of intracranial aneurysms: a systematic review. *Stroke*, 29: 251-259, 1998.

Ropper, A. H. and N. T. Zervas. Outcome 1 year after SAH from cerebral aneurysm. Management morbidity, mortality, and functional status in 112 consecutive good-

risk patients. *Journal of Neurosurgery*, 60: 909-915, 1984.

Sforza, D., C. M. Putman, et al. Hemodynamics of Cerebral Aneurysms. *Ann Rev Fluid Mechanics*, 41: 91-107, 2009.

Shojima, M., M. Oshima, et al. Magnitude and role of wall shear stress on cerebral aneurysm: computational fluid dynamic study of 20 middle cerebral artery aneurysms. *Stroke*, 35(11): 2500-2505, 2004.

Tsutsumi, K., K. Ueki, et al. Risk of rupture from incidental cerebral aneurysms. *Journal of Neurosurgery*, 93: 550-553, 2000.

Valencia, A., H. Morales, et al. Blood flow dynamics in patient-specific cerebral aneurysm models: the relationship between wall shear stress and aneurysm area index. *Med Eng Phys*, 30(3): 329-40, 2008.

Weir, B. and R. L. Macdonald. Intracranial aneurysms and hemorrhage: an overview. *Neurosurgery*. R. S. Wilkins RH. New York, McGraw-Hill**:** 2191-2213, 1996.

Wiebers, D. O., J. C. Torner, et al. Impact of unruptured intracranial aneurysms on public health in the United States. *Stroke*, 23: 1416-1419, 1992.

Wiebers, D. O., J. P. Whisnant, et al. International Study of Unruptured Intracranial Aneurysms Investigators. Unruptured intracranial aneurysms: natural history, clinical outcome, and risks of surgical and endovascular treatment. *Lancet*, 362(9378): 103-110, 2003.